Measuring the Nonuniform Evaporation Dynamics of Sprayed Sessile Microdroplets with Quantitative Phase Imaging

Chris Edwards,[†,‡] Amir Arbabi,[†,‖] Basanta Bhaduri,[‡] Xiaozhen Wang,[†] Raman Ganti,[§,⊥] Peter J. Yunker,[§,#] Arjun G. Yodh,[§] Gabriel Popescu,[‡] and Lynford L. Goddard*,[†]
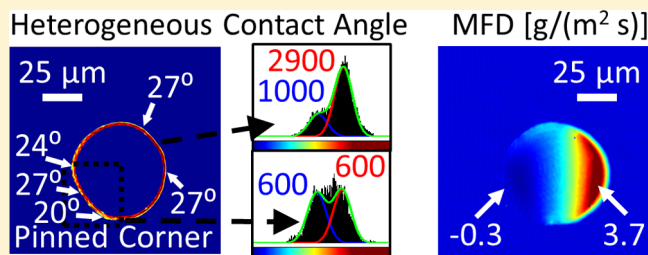
[†]Photonic Systems Laboratory, Micro and Nanotechnology Laboratory, Department of Electrical and Computer Engineering, University of Illinois at Urbana−Champaign, Urbana, Illinois 61801, United States

[‡]Quantitative Light Imaging Laboratory, Beckman Institute for Advanced Science and Technology, Department of Electrical and Computer Engineering, University of Illinois at Urbana−Champaign, Urbana, Illinois 61801, United States

[§]Department of Physics and Astronomy, University of Pennsylvania, Philadelphia, Pennsylvania 19104, United States

Ⓢ *Supporting Information*

ABSTRACT: We demonstrate real-time quantitative phase imaging as a new optical approach for measuring the evaporation dynamics of sessile microdroplets. Quantitative phase images of various droplets were captured during evaporation. The images enabled us to generate time-resolved three-dimensional topographic profiles of droplet shape with nanometer accuracy and, without any assumptions about droplet geometry, to directly measure important physical parameters that characterize surface wetting processes. Specifically, the time-dependent variation of the droplet

height, volume, contact radius, contact angle distribution along the droplet's perimeter, and mass flux density for two different surface preparations are reported. The studies clearly demonstrate three phases of evaporation reported previously: pinned, depinned, and drying modes; the studies also reveal instances of partial pinning. Finally, the apparatus is employed to investigate the cooperative evaporation of the sprayed droplets. We observe and explain the neighbor-induced reduction in evaporation rate, that is, as compared to predictions for isolated droplets. In the future, the new experimental methods should stimulate the exploration of colloidal particle dynamics on the gas−liquid−solid interface.

I. INTRODUCTION

The dynamics of microdroplet surface wetting and evaporation are subjects of extensive study in the fields of physics, chemistry, and engineering. Applications of interest include microfluidics,[1,2] mechanical lubrication,[3] water-resistant and self-cleaning surfaces,[4,5] spray cooling,[6] reflow of photoresist,[7] thin-film deposition,[8−10] self-assembly of nanoparticles,[11] biochemical assays,[12] deposition of DNA/RNA microarrays,[13] fabrication of advanced materials[14] and dissolvable electronics,[15] and printing using inkjet[16] and electrohydrodynamics jet[17] technologies. In many of these applications, the first process step involves spraying microdroplets onto a solid surface. Therefore, measurement of droplet surface wetting and evaporation dynamics of sprayed droplets would be of great value for understanding and further developing a variety of high-yield industrial processes.

Presently, there are several methods available for the characterization of surface wetting and evaporation. Among these, the sessile droplet or goniometric method[18−22] is the most widely used. This basic technique employs a syringe oriented perpendicular to a substrate to place a single, isolated droplet of a predetermined volume. The receding and advancing contact angles can be measured by siphoning or depositing more liquid. Once the droplet is in place, a high-resolution image of the droplet is taken from the side, and image analysis software is employed to compute the height, contact radius, and contact angle. When a liquid droplet is sufficiently small and surface tension dominates over gravity, which corresponds to the small angle limit, the spherical cap approximation (SCA) can be used to derive other droplet parameters.[18−20] When it comes to a wide angular range, Frenkel's method can be applied to obtain a relation between the edge velocity and the dynamic contact angle for both complete and partial spreading.[21] When the droplet evaporates on a solid surface in constant contact angle mode and an initial angle of less than 90°, Erbil et al. have found that the decrease of the square of the contact radius of the droplets was linear with time.[22] Although these methods can derive droplet parameters, they only use the contact angle and contact radius measurements obtained from a single viewing angle. In practice, there can be variations in these parameters around the droplet's perimeter. Further, the goniometric technique also has some

A

difficulty resolving small contact angles (<10°) and micro- and nano-sized droplets in general. The small flat droplet issue has been studied for years.[23−26] Hu et al.[23] derived a simple approximate evaporation rate expression, which agreed with the theoretical results[24,25] for any initial contact angle between 0° and 90°. Guena et al.[26] demonstrated that a wedge model accounted very well for a droplet with very small contact angles (a few degrees or less) and receding motion.

In a different vein, scanning white light interferometry has been employed to record the profiles of isolated droplets near the contact line. In this case, interference fringes are recorded while scanning over the specimen; this information can then be used to produce a three-dimensional profile of the droplet.[27] Vertical scanning, however, is time-consuming, and therefore this method is only suitable for the study of very slowly evaporating droplets. Another imaging technique measures the reflectivity of the liquid film at each pixel location along the entire droplet profile and from these data derives droplet shape.[28] This approach utilizes gray scale plots of the naturally occurring interference fringes that result from reflection of light at the liquid−vapor and solid−liquid interfaces to obtain thickness profiles for the droplets; the curvature and apparent contact angle are then calculated from best fits to the experimental thickness profile. Laser light interference microscopy techniques have been employed to study the dynamics of liquid droplet spreading. In this case, a movie of the interferometer fringes enabled the spreading speed at the droplet edge to be measured and the edge profile to be reconstructed.[29] Because these techniques involve fitting to a prescribed droplet shape, deviations from the ideal shape will inevitably lead to errors. Reflectance interference microscope (RIM) was developed to accurately extract the full thickness profile of an air layer trapped between a droplet and a solid surface. A high-speed dual wavelength RIM system with an unprecedented resolution of ∼10 nm and 50 μs was demonstrated.[30] RIM can be used to investigate bubble entrapment and deformation.[31] The RIM technique requires an optical cavity (i.e., a low refractive index air bubble sandwiched between the high index droplet and glass or a high index material between two low index ones) to form interference fringes. RIM only provides thickness information for the middle material. Thus, RIM can only measure the properties of a droplet on a substrate in air when the droplet has a higher index than the substrate.

Other advanced techniques, such as fluorescence microscopy, have been successfully developed to study the profiles of droplets in dynamic wetting. Typically, the specimen is marked with a fluorescent molecule and illuminated with light of a specific wavelength. The fluorescent molecule, or the fluorophore, absorbs this incident light and emits light of a longer wavelength. Fluorescence microscopy is particularly powerful in the vicinity of the contact line. H. P. Kavehpour and his co-workers developed very successful methods to use fluorescence microscopy for examining the precursor films of spreading droplets.[32,33] This technique has the ability to measure very thin films with sufficient range, resolution, and signal-to-noise ratio, in a noninvasive manner. Additionally, the high spatial and temporal resolution of this optical technique allows a wide range of dynamic applications. However, this technique requires the specific structures to be labeled for fluorescence, and the total observation time is severely limited by photobleaching.

Atomic force microscopy (AFM) provides a nanometer-resolution three-dimensional surface profile of the sample without any special treatments. AFM has a variety of operational modes, such as contact mode, noncontact mode, tapping mode, and scanning polarization force microscopy. T. Pompe and S. Herminghaus used AFM in tapping mode to image the topography of liquid sessile droplets and determine contact line tension.[34] F. Mugele et al. imaged nanometer scale liquid droplets using AFM to study droplets that were several orders of magnitude smaller than what can be measured with conventional goniometric methods.[35] By analyzing the global shape of the liquid−vapor interface of micrometer-sized droplets, their measurements revealed that the strong droplet size dependence of the contact angle is not caused by the line tension. A. Checco et al. reported a dynamic (also called noncontact) AFM technique for imaging droplets directly condensed onto solid surfaces.[36] The setup achieves true noncontact profiling, thus ensuring a very low degree of sample perturbation as compared to tapping mode. The wetting contact angle can be directly accessed from AFM topography. This method allows for spatial variations of the substrate wettability to be evidenced by recording nanoscale distortions of the liquid contact line and its behavior of hysteresis. Despite these advanced characterization capabilities, AFM has the obvious disadvantage of being a serial inspection method and thus offers a limited scanning speed.

Environmental scanning electron microscopy (ESEM) enables samples to be measured at high resolution without the sample environment needing to be at high vacuum.[37] In addition, wet and nonconductive samples can be examined by using a gaseous environment in the specimen chamber. This technique has also been utilized to look at droplet condensation and evaporation dynamics, especially contact line movement. K. Rykaczewski studied sub-10 μm dynamics of droplet formation in the constant base area mode on nanostructured superhydrophobic surfaces using ESEM and at a 10−50× faster image acquisition rate versus previous research.[38] A. T. Paxson and K. K. Varanasi applied the ESEM approach to the specific situation of superhydrophobic surfaces and revealed a self-similar mechanism of the receding contact line of nonwetting drops at micron length scales.[39] Recently, Q. Liu et al. visualized the depinning dynamics of water nanodroplets from gold nanoparticles on a flat substrate using in situ transmission electron microscopy (TEM) imaging.[40] Two challenges associated with ESEM and in situ TEM are that they typically require specialized sample preparation and they can perturb evaporation dynamics (e.g., the imaging beam can be used to induce droplet movement[40]).

In this Article, we demonstrate diffraction phase microscopy (DPM), a quantitative phase imaging (QPI) method that uses fast field retrieval algorithms[41−43] for the real-time calculation of the three-dimensional topographic profiles of surface wetting and evaporation. The technique provides direct time-dependent measurements of droplet height, contact radius, volume, surface area, radius of curvature, mass flux density, and contact angles around the entire droplet perimeter throughout the evaporation process. DPM is an emerging technology that measures shifts in the optical path-length created by the sample at each point in the image; this information enables reconstruction of surface topography with better than 0.5 nm accuracy in height[44] and diffraction-limited submicrometer transverse resolution. The technique has been employed with success in a variety of contexts[41,44−50] and has enabled new studies in biomedicine

over the past decade.[51] Here, we show how quantitative phase imaging enables full three-dimensional reconstruction of the droplet shape during evaporation. In the process, we directly observe a variety of phenomena that occur during droplet evaporation, including nonuniformities in the contact angle, time-dependent and heterogeneous pinning and depinning, as well as the effects of cooperative droplet evaporation on drying dynamics.
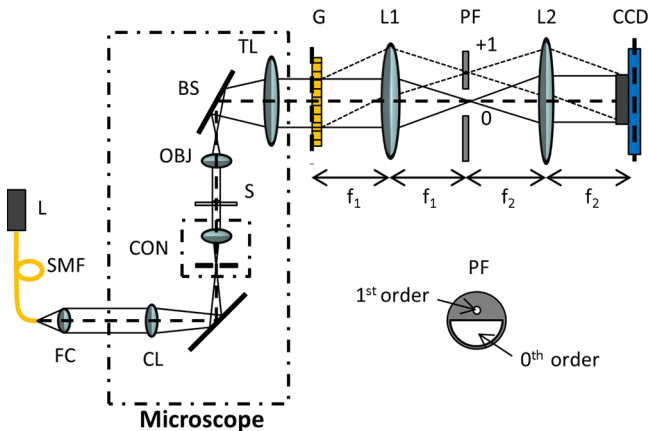

Figure 1. Experimental setup for DPM imaging system. Abbreviations: L, laser; SMF, single mode fiber; FC, fiber collimator; CL, collector lens; CON, condenser; S, sample; OBJ, objective; BS, beam splitter; TL, tube lens; G, grating; L1/L2, lenses; PF, pinhole filter; CCD, charge-coupled device.

II. EXPERIMENTAL SETUP

DPM is a particular approach to QPI characterized by very high stability, because it relies on a common-path interferometer.[47,48,52,53] For the present problem, we developed a high-resolution transmission DPM system to study the evaporation of sprayed microdroplets on glass substrates. Figure 1 shows the setup for our experiments. The illumination source is an Nd:YAG frequency-doubled laser operating at 532 nm. The laser light is coupled into a single-mode fiber and then collimated. The collimated beam enters the back port of the microscope, passes through the collector lens, and is focused at the front focal plane of the condenser, where the condenser aperture is left completely open. The condenser lens then produces a collimated beam at the sample plane. The light passes through the sample containing the evaporating water droplet, is collected through the objective, and is focused onto its back focal plane. A beam splitter directs the light through a tube lens so that it is again collimated at the output image plane of the microscope. The beam splitter also directs light into an eyepiece (not shown).

A diffraction grating (Thorlabs, GT25-03, a visible transmission grating with 300 grooves/mm and 17.5° blaze angle) is placed at the output image plane of the microscope such that multiple copies of the image are generated at different angles. Some of the orders are collected by the first lens (L_1), which is placed a focal length f_1 away from the grating, producing the Fourier transform of the image at a distance f_1 behind the lens. Here, all of the diffraction orders are blocked, except for the zeroth and the positive first. The first-order beam is blocked except for its zero wavevector component ($k = 0$) using a 10 μm diameter pinhole, such that after passing through the second lens (L_2) this field approaches a plane wave. This beam serves as the reference beam for the interferometer. A large semicircle permits the full zeroth order to pass through the filter without introducing additional windowing effects. Using the zeroth order as the image also prevents unnecessary aberrations because it passes through the center of the lenses along the optical axis. A blazed grating is employed where the positive first order is brightest. This way, after
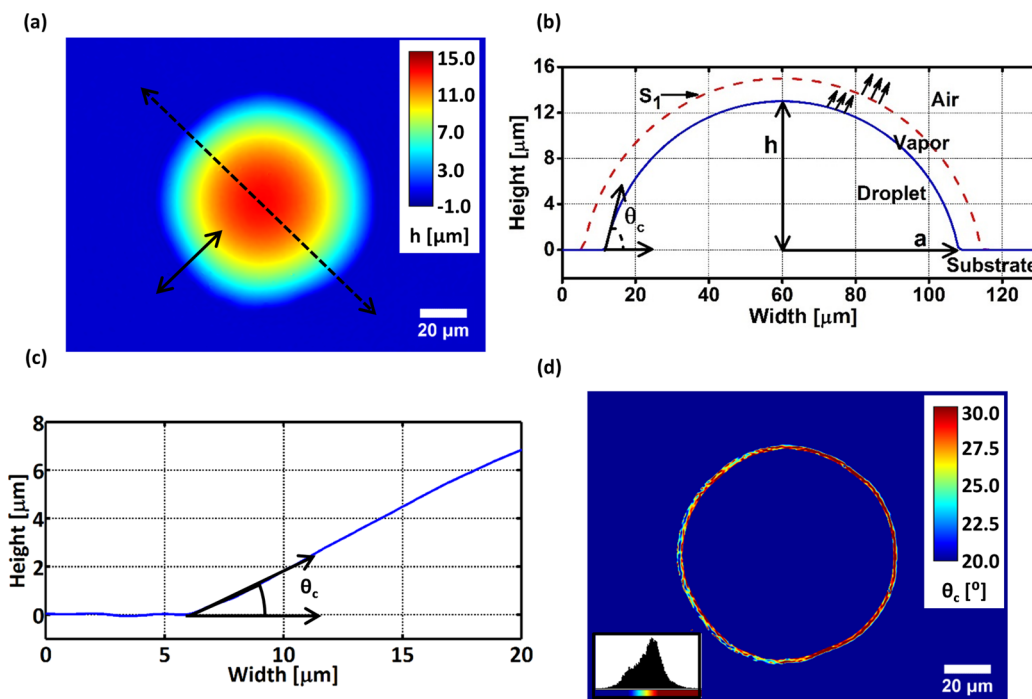

Figure 2. Direct measurements of a water droplet during evaporation. (a) DPM height profile. (b) Cross-sectional profile taken along the dotted line in (a). Height, contact radius, and contact angle can be measured directly from the quantitative phase image. S_1: Evaporation occurs across surface 1 (red boundary). (c) Zoomed-in portion of profile taken along solid line in (a). Contact angles can be measured directly at any point around the droplet's edge. (d) Masked gradient angle profile displaying all contact angles. The inset in (d) contains the histogram, which readily gives the mean, median, interquartile range, mode, standard deviation, and many other statistics about the contact angles around the entire droplet.
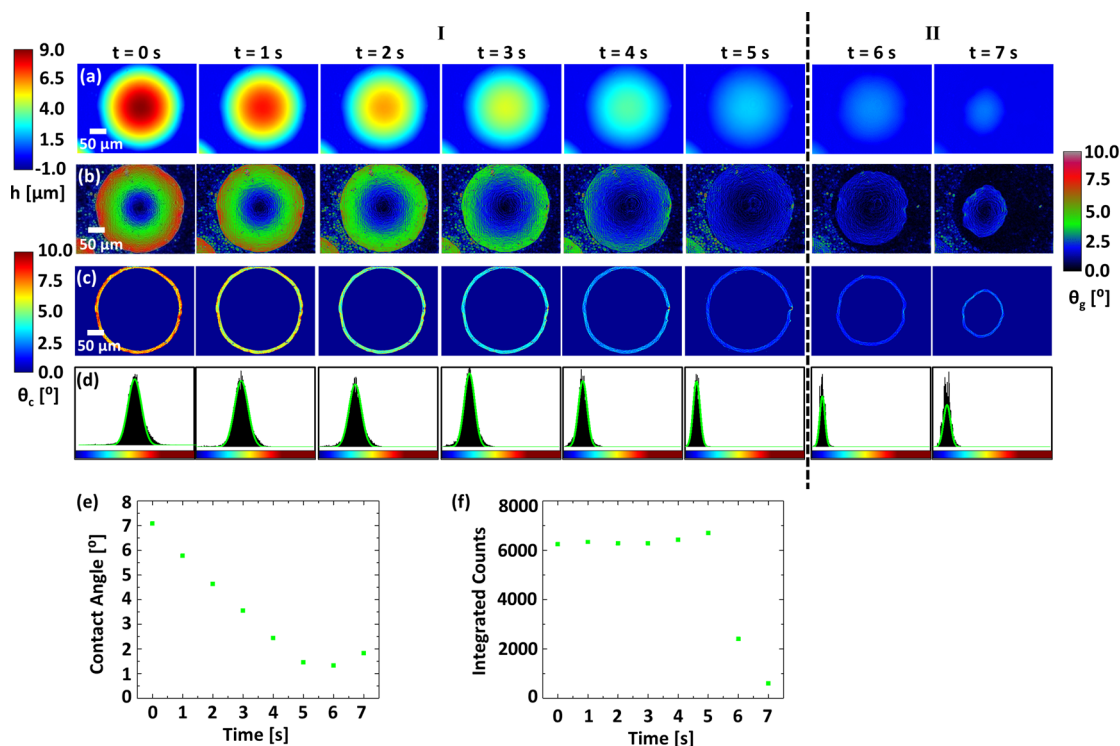
Figure 3. Pinned−depinned transition on treated glass. (a) DPM height, h, map, (b) gradient angle, θ_g, map, (c) contact angle, θ_c, map, (d) corresponding histograms of the contact angle maps with single Gaussian peak fits, (e) mean contact angle of the fits, and (f) integrated counts of the fit (i.e., the area under the Gaussian curve). The field of view is 360 μm × 270 μm. The evaporating droplet undergoes a clear transition from the constant contact area mode to the constant contact angle mode at around 5.2 s. Region I in (a)−(d) indicates the constant contact area regime, and region II indicates the constant contact angle regime.
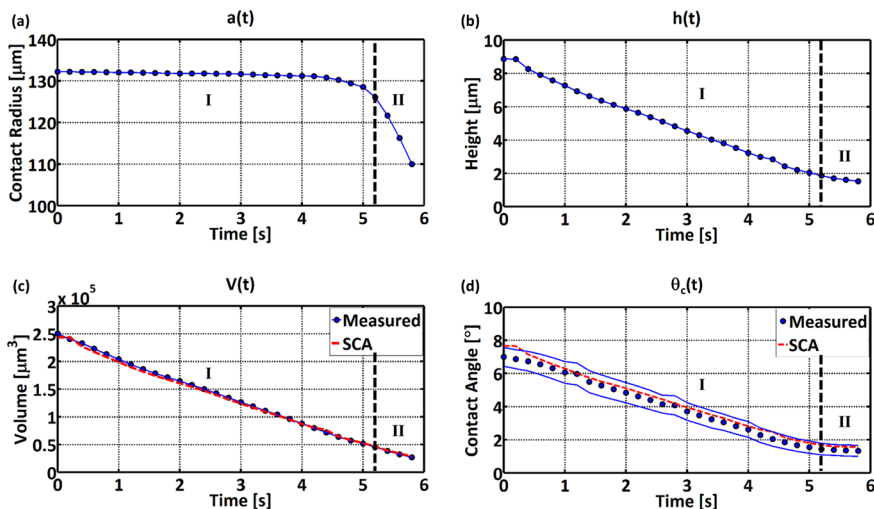

Figure 4. Evaporation dynamics during the pinned−depinned transition. Time evolution of (a) contact radius and (b) height. (c) Comparison of the directly measured volume and the volume computed using SCA with the height and contact radius data. (d) Corresponding comparison for contact angle. The measured data in (d) show the median contact angle (symbols) and the 25th and 75th percentiles of the contact angle distribution (lines). In region I, the contact radius is almost constant, but the height and contact angle decrease in a nearly linear fashion. The receding angle is reached and depinning occurs around 5.2 s. I indicates the constant contact area regime, and II indicates the constant contact angle regime.

the filter, the intensities of the two orders are closely matched, ensuring optimal fringe visibility. A second 2f system with a different focal length f_2 is utilized to perform another spatial Fourier transform producing the image at the charge-coupled device (CCD) plane. The two beams interfere to produce an interferogram at the camera plane (Zeiss AxioCam MRm CCD). This interferogram is a spatially modulated signal from which we can extract the phase information via a Hilbert transform and reconstruct the surface profile.[41,54] A background image is first taken from a portion of the substrate containing no droplets and then used to subtract the background noise from all subsequent images.[41,54] In this Article, the substrate is homogeneous; however, our method can be extended to the more general case of a textured or chemically heterogeneous surface if a background image is taken from the same location prior to droplet spraying. Following the phase reconstruction, we perform an unwrapping routine based on the Goldstein algorithm. The quantitative phase images captured by this approach enable us to acquire a full three-dimensional description of evaporating droplets at

each moment in time. The performance of our DPM system can be further improved by using a higher numerical aperture (NA) objective lens to enhance the lateral resolution, by increasing the pixel count of the camera to expand the field of view, and by increasing the frame rate of the camera to capture even faster evaporation dynamics.

To better replicate typical droplet deposition processes found in industrial applications, droplets of distilled water are sprayed onto the substrate using a fine mist spray bottle. Because we can directly measure the volume by imaging, there is no need to pipet a single droplet of predetermined volume onto the substrate as in the sessile droplet method. Furthermore, we are not limited by the assumption that the droplet is spherical because we can characterize droplets of arbitrary shape. Once the sample is prepared, a time-lapse series is recorded, which reveals the dynamics of the evaporation process. All time lapses were taken with a 40 ms exposure time and a 200 ms acquisition period. A top-down view of the topographical height map obtained via DPM is shown in Figure 2a. Figure 2b shows the cross-sectional profile taken along the dotted line in Figure 2a, which illustrates how we can directly measure the height, contact radius, and contact angle from any arbitrary cross-section of the droplet. Figure 2c displays a zoomed-in view of the droplet's edge, which is shown as a solid line in Figure 2a. Here, the contact angle can be extracted using a tangent fit.[55] The accuracy of our contact angle measurements was verified by imaging a commercial fused silica microlens array that has contact angles below 2° (see Figure S1[56]). From the droplet profile data, we are able to directly measure many of the important parameters required to understand the wettability of particular liquid/substrate combinations.

To further characterize the evaporation process, we computed the gradient angle map by taking the gradient of the height image and computing the angle between the gradient vector and the $x-y$ plane. The gradient angle at the droplet's edge gives the contact angle. Thresholding and binary masking the image based on both height and angle information enabled us to easily identify the perimeter of the droplet. Figure 2d shows a map of contact angles. The resulting histogram shown in the inset reveals the mean, median, interquartile range, mode, and standard deviation of the contact angles around the entire droplet. Clearly, an abundance of statistical information is acquired with this technique. Moreover, the height (h), contact radius (a), contact angle (θ_c), volume (V), surface area (SA), radius of curvature (R), and mass flux density (MFD) can be determined during evaporation via direct measurements of the droplet topography as a function of time. In addition to providing insights into the dynamics of droplet evaporation, MFD measurements are also valuable to the understanding of many biological processes. Cellular dry mass, which is defined as the nonaqueous content of a cell, can be studied by using interferometric quantitative phase microscopy.[57,58] We define MFD = $\rho(\mathrm{d}h/\mathrm{d}t)$, where ρ is the density of the liquid (water). For water, we have $\rho = 997$ kg/m^3. Because the accuracy of our height measurement is approximately 0.5 nm and our frame rate is 5 frames/s, we have a sensitivity for $\mathrm{d}h/\mathrm{d}t$ of 2.5 nm/s and for MFD of 2.5×10^{-6} kg/(m$^2 \cdot$s) at each pixel. MFD includes all processes that change the droplet's shape, for example, diffusive evaporation and mass redistribution within the droplet due to radial convection. The evaporation process, which does not include convection, causes water vapor to cross the surface (S_1) of Figure 2b. Theory on the evaporative flux density (J) will be presented later. We will compare theory to experiment by integrating J over S_1 and integrating MFD over the droplet's cross-sectional area in the $x-y$ plane because, according to the continuity equation (i.e., conservation of material), each of these integrals will be equal to the rate of decrease of the droplet's total mass ($-\mathrm{d}m/\mathrm{d}t$):

$$-\frac{\mathrm{d}m}{\mathrm{d}t} = -\rho \frac{\mathrm{d}V}{\mathrm{d}t} = \int_{S_1} J \cdot \mathrm{d}S = \int \mathrm{MFD}(x, y) \, \mathrm{d}x \, \mathrm{d}y \quad (1)$$

III. RESULTS AND DISCUSSION

It is well documented that droplet evaporation occurs in three distinct phases.[24,59−61] In the initial stage, known as the constant contact area mode (stage I), the contact line is pinned

and the contact angle decreases linearly with time. Within this regime, radial convection occurs within the droplet to compensate for uneven evaporation along the surface of the droplet. When the droplet contact angle reaches the so-called receding angle, it can no longer produce the required radial flow to maintain equilibrium given its diminishing volume.[62] This situation effectively leads to a depinning of the droplet boundaries and to the second phase of the evaporation process, which is sometimes referred to as the constant contact angle mode (stage II). During this stage, the contact angles remain nearly constant, the mass flux density is nearly uniform, and the radial convection is minimal.[24,59,60] Finally, as the evaporating droplet becomes very small, imperfections in the substrate become important, and the droplet enters a mixed mode, sometimes referred to as the drying mode (stage III), wherein both the contact radius and the contact angle recede rapidly. It is believed that for an ideal substrate (perfectly flat and impurity-free), the constant contact angle mode (stage II) will persist until complete evaporation has taken place.[55]

A time lapse sequence of DPM images of an evaporating water droplet sprayed onto a treated glass substrate was taken at a rate of 5 frames/s. The substrate was treated with ethanol and burned to achieve a more hydrophilic surface and to encourage a smooth transition between phases I and II. A 5× objective was used for imaging, providing a 360 μm × 270 μm field of view. Figures 3 and 4 show the dynamic measurements as the droplet transitions from a pinned state to a depinned state during evaporation. Figure 3a shows selected frames of the height map images. Movie M1[56] is the full video of the height images. The initial volume, height, and contact radius of the droplet were 2.50×10^5 μm^3, 8.87 μm, and 132 μm, respectively. The droplet is initially in the pinned state, and it remains in this regime until the receding angle of 1.28° is reached after 5.2 s of evaporation.

The second row of images (Figure 3b) contains the corresponding gradient angle maps. The corresponding video (movie M2) is viewable in the Supporting Information.[56] The third row of images (Figure 3c) contains the contact angle maps. Movie M3 shows the corresponding contact angle maps.[56] The fourth row of images (Figure 3d) contains the histograms of contact angles corresponding to the images in Figure 3c. Movie M4 shows the corresponding histograms.[56] The histograms in Figure 3d fit well to a single Gaussian peak because the contact angles were relatively homogeneous around the droplet edge. This wealth of statistical information enables us to quantify the degree of homogeneity of the droplet's contact angles and is a unique capability of the measurement technique. Figure 3e shows the mean contact angle of the fit, which shows that the contact angles are measurable below 2°. As derived in the Supporting Information,[56] the maximum measurable contact angle is determined by the objective NA and the refractive indices of the liquid and the ambient by requiring that all light refracted by the droplet be collected by the objective. The result is that $\theta_{\max} = 20.8°$ for our 5×/NA = 0.13 objective, $\theta_{\max} = 30.4°$ for our 10×/NA = 0.25 objective, and that the maximum angle for DPM can be 90° if the collimated light enters the droplet from the curved top surface (a lensing effect) rather than the flat bottom surface, assuming an objective with NA > 0.883 is used (e.g., 40×/NA = 0.95). Figure 3f shows the integrated counts of the fit (i.e., the area under the Gaussian curve). There are y-error bars in the Figure 3e and f plots that represent the standard error (SE) of these fit parameters, but they are smaller than the markers. The
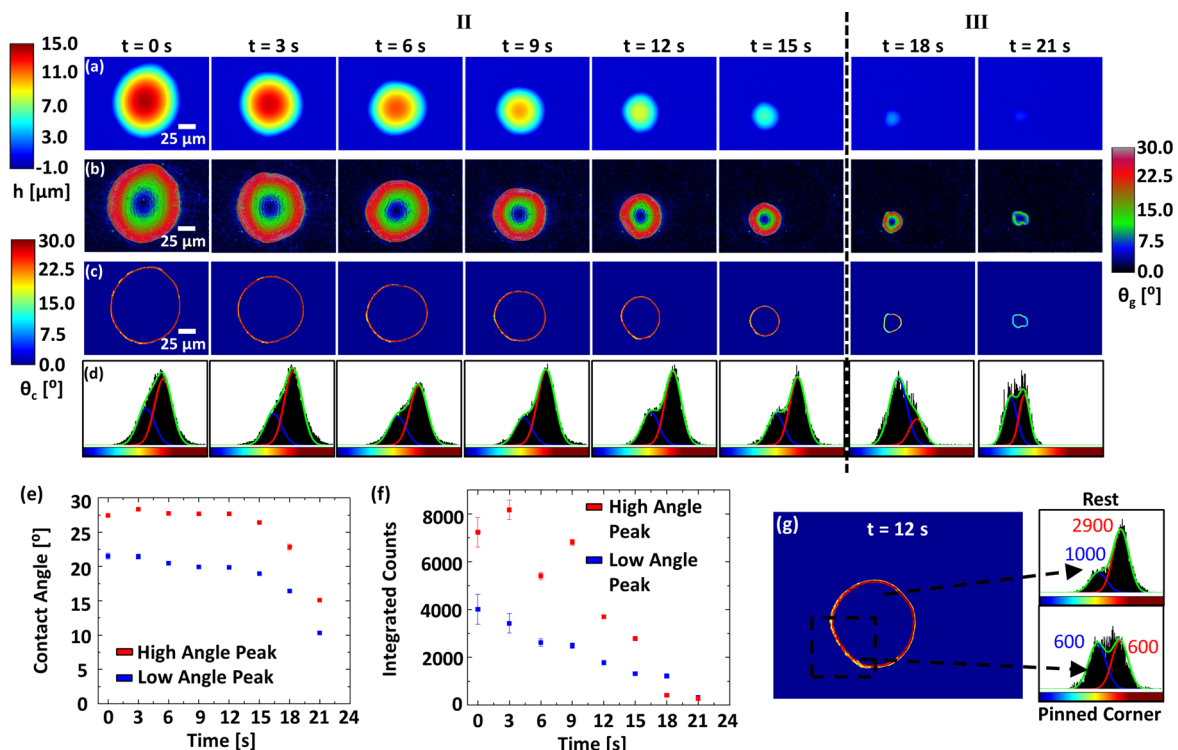
Figure 5. Partial pinning on untreated glass. A sequence of DPM images of an evaporating water droplet on an untreated glass coverslip was taken at 5 frames/s using a 10× objective resulting in a 180 μm × 135 μm field of view. The droplet exhibits partial pinning in the lower left-hand corner. A subset of these images showing the (a) DPM height map, (b) gradient angle map, (c) contact angle map, (d) corresponding histograms of the contact angle maps with double Gaussian peak fits, (e) mean contact angles of the fits, (f) integrated counts of the fits, and (g) separated histograms for the fully pinned region (indicated by dotted box) and the rest of the image. The transition from constant contact angle mode into the drying phase is observed after 16.4 s. II indicates the constant contact angle regime, and III indicates the drying phase.
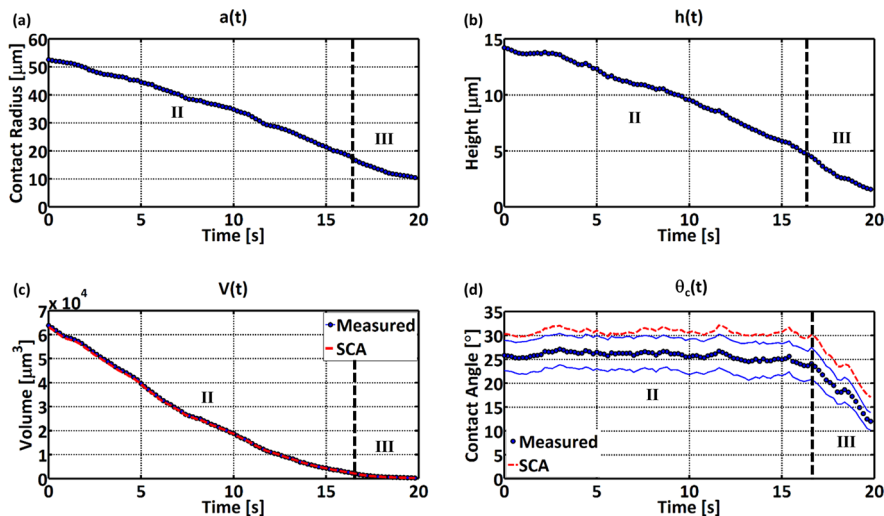

Figure 6. Evaporation dynamics during partial pinning. Time evolution of (a) contact radius and (b) height. (c) Comparison of the directly measured volume and the volume computed using the SCA with the height and contact radius data. (d) Corresponding comparison for contact angle. The measured data show the median contact angle (symbols) and the 25th and 75th percentiles of the contact angle distribution (lines). In phase II, the contact angle averaged over the entire droplet is almost constant, but the height and contact radius decrease in a nearly linear fashion. The drying phase occurs around 16.4 s. II indicates the constant contact angle regime, and III indicates the drying phase.

integrated counts are nearly constant when pinned because the contact edge in Figure 3c is not changing. The integrated counts decrease as the droplet evaporates inward.

The dynamic measurements of the droplet contact radius (*a*), height (*h*), volume (*V*), and contact angle (θ_c) for the time lapse sequence are presented in Figure 4a−d, respectively. In

frames 1−26 (0−5.2 s), the contact angle decreases linearly with time, which can be observed as the colors in Figure 3c at the droplet edge change at a constant rate. After depinning occurs (i.e., frame 27 on), the contact angle barely changes and the colors in Figure 3c at the edge of the droplet remain nearly constant. Further, the contact radius starts to decrease at
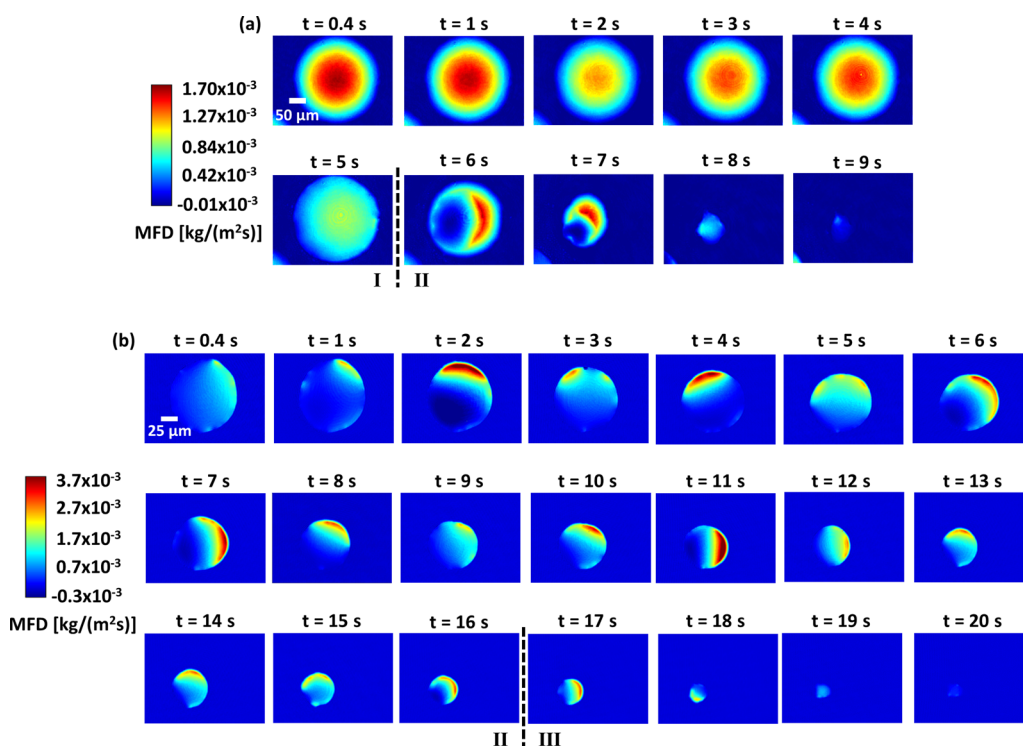
Figure 7. Mass flux density. (a) Mass flux density of the pinned−depinned treated glass case (from Figure 3) as a function of *x*, *y*, and *t*. Note that at *t* = 5.2 s, the droplet depins, but the lower left corner does not depin in the same manner as the rest of the droplet due to screening effects from the neighboring droplet seen in the lower left corner. (b) Mass flux density for the partial pinning untreated glass case (from Figure 5).

approximately the same time. Together, these effects are indicative of the second phase of evaporation, that is, the constant contact angle mode.[24,59,60]

In the pinned regime, the volume, height, and contact angle all decrease at nearly constant rates. This behavior is a result of the pinned boundary conditions and the nonuniform mass flux density.[24,60] The contact radius versus time plotted in Figure 4a clearly indicates the transition from phases I to II, wherein depinning occurs. The measured volume and median contact angle are also compared to the SCA; in this case, we use height and contact radius data to compute the SCA parameters. Notice that although deviations in volume are small, the SCA tends to overestimate the contact angle, which is an important parameter for the determination of the surface tension.

Next, to show that the DPM technique can handle more real world conditions, evaporation of a droplet from an untreated glass coverslip substrate was investigated. A 10× objective was used, which resulted in a field of view of roughly 180 μm × 135 μm. Figures 5 and 6 show the corresponding dynamic measurements of this partially pinned microdroplet. To appreciate these behaviors, see the corresponding height movie M5, gradient angle movie M6, contact angle movie M7, and histogram movie M8.[56] The initial volume, height, and contact radius of the droplet were 6.38 × 10^4 μm^3, 14.21 μm, and 53 μm, respectively.

Interestingly, this particular droplet exhibits partial-pinning. The lower left corner of the droplet (dotted rectangle region in Figure 5g) is fully pinned and does not move during phase II (constant contact angle). However, as can be seen in movie M7,[56] the droplet boundary outside the rectangular box does not recede inward uniformly. Instead, at different moments in time during phase II, various parts of the boundary appear to be pinned and depinned. The overall motion of the boundary is

not uniform; the fully pinned contact line in the lower left corner appears to pull the center of the droplet toward the lower left corner during evaporation. We suspect that the observed overall partial-pinning is due to a slowdown in the evaporation rate because of a nearby droplet from the spray. Other possible causes of partial-pinning are the surface roughness and the chemical heterogeneity of the untreated glass coverslip.[60,63]

As a result of partial pinning, the histograms in Figure 5d were asymmetric; we were unable to fit these distributions with a single Gaussian peak. Instead, the data were fitted to a sum of two Gaussians to quantify the heterogeneity of the contact angles during partial pinning. The blue and red Gaussians represent the low and high contact angle peaks, respectively. Figures 5e and f show the respective mean contact angles and integrated counts for each peak. There is greater uncertainty in these parameters than in Figure 3, which makes the *y*-error bars more visible. The contact angle maps in Figure 5c clearly indicate two separate droplet regions along the circumference. The lower contact angles tend to reside more in the fully pinned lower left corner. As the droplet evaporates, the integrated counts for the low and high angle peaks decrease and become comparable once the droplet enters the drying phase. Figure 5g shows separate histograms at *t* = 12 s for the fully pinned dotted rectangle region and for the rest of the image. These two histograms are fitted to the double Gaussian sum, using the same mean and standard deviation as the fit in Figure 5d for *t* = 12 s to determine the integrated counts for each peak. The integrated counts for the fits are labeled as color text in Figure 5g. It is clear that the pinned region exhibits a significantly different distribution of contact angles when compared to the rest of the droplet. The average contact angle is larger in the partially pinned region than in the fully

pinned lower left corner. The droplet behavior can be understood by considering multiple substrate regions that have different receding contact angles due to the heterogeneous surface properties of the untreated substrate. When the initial contact angle of the droplet is larger than the largest receding angle, the droplet is in the fully pinned phase of evaporation. During evaporation, the contact angle decreases more or less uniformly everywhere. When the contact angle decreases to the largest receding angle, the contact line in the corresponding region will depin first, and its contact angle will remain constant at the value of the largest receding angle. The contact angle in the other regions can continue to decrease, which creates a partial pinning state. The average contact angle in the depinned region is therefore higher than that in the pinned region. Eventually, all regions reach their corresponding receding angle, and the droplet becomes fully depinned. After 16.4 s of evaporation, the droplet enters the drying mode where the contact radius and angle recede rapidly. From the gradient angle image sequences for both droplets (see especially Figure 3b), it can be observed that the background where the droplet initially resided remains clean during evaporation. Thus, we believe that the heterogeneous property of the glass is due to impurities on the untreated substrate. As the droplet moves inward, it traps impurities from the surface and complicates the evaporation dynamics. As can be seen in Figures 6c and d, the SCA provides a good estimate of the volume, but significantly overestimates the contact angle. This discrepancy is more pronounced for the untreated glass case because of the greater variation in contact angle along the perimeter. It is noteworthy to mention that instances of partial pinning are difficult to observe and impossible to characterize when using the sessile droplet or goniometric technique, because these methods only produce a side view.

IV. MASS FLUX DENSITY

Figure 7a shows selected frames of the mass flux density of the droplet from Figures 3 and 4 as a function of x, y, and t. The full video (movie M9) is available in the Supporting Information.[56] Theory predicts that the evaporative flux density is nonuniform with maxima along the droplet's edge.[54] Interestingly, however, during the pinned phase of evaporation, the mass flux density has a maximum at the center of the droplet with minima along the droplet's edge to satisfy the pinned boundary condition. This suggests that radial convection occurring within the droplet is pushing mass from the center to the droplet's edge. In other words, flow patterns within the droplet will move fluid from the red regions to the blue regions of Figure 3a. This phenomenon produces the well-known "coffee ring" effect. The total flux decreases with volume of the droplet until depinning occurs. Once depinned, however, the droplet does not continue to evaporate in a concentric manner as theory would suggest. Depinning actually occurs at different time-points around the edges, and the lower left corner depins much later than the rest of the droplet. This phenomenon may be due to evaporation slowdown effects caused by the neighboring droplet seen in the lower left corner of the image. Partial pinning effects, such as these, affect the evaporation rate. Figure 7b shows the mass flux density for the droplet depicted in Figures 5 and 6. See the mass flux movie M10.[56] Again, the minimum change in volume occurs along the pinned edge located in the lower left-hand corner. Further, there are regions of negative mass flux density near this pinned edge at $t = 2$ s and also at several other time frames, indicating that the droplet is actually gaining mass in

this region of space during evaporation. This behavior is a result of momentum conservation: fluid in the droplet is pushed toward the pinned edge because of the faster evaporation from the depinned edge. The maximum in the mass flux density rotates back and forth around the depinned edge of the droplet, suggesting that convective flows within the droplet are moving fluid from depinned regions to pinned regions in a complicated manner. The motion of the droplet's mass is that of a propagating fluid wave that reflects off of a pinned boundary.

V. THEORETICAL MODELS

Several theoretical models have been developed to describe the evaporation of an isolated spherical cap droplet. In 1977, Picknett and Bexon[24] described the three modes of evaporation, which are constant contact area (pinned), constant contact angle (depinned), and a mixed mode (combination of pinned and depinned). They developed isothermal diffusion theory models to describe the evaporation in both the pinned and the depinned cases separately. The final regime, referred to as the mixed or drying mode, is highly complicated and depends on several effects, which are difficult to model for the arbitrary case. Picknett and Bexon introduced the so-called $f(\theta_c)$ factor (θ_c is the contact angle) to account for the presence of the substrate, which hinders the evaporation process. Simpler versions of the $f(\theta_c)$ factor were made by Shanahan[60] and Rowan[64] in subsequent years, but these approximations are only valid for larger contact angles.

In 2011−2012, Nguyen and co-workers solved Fick's second law (i.e., the diffusion equation) in steady state (i.e., Laplace's equation) in toroidal coordinates and developed an analytic expression for the net diffusive flux of a single sessile droplet.[65,66] The problem is analogous to finding the electrostatic field strength at the surface of a lens-shaped conductor that is held at potential V_0 relative to ground at infinity. Their model is valid for both pinned and depinned modes, and they presented a simplified equation for each case. We will build upon their general expression to analyze the evaporation rate of densely sprayed droplets for both modes. Their key result was that the net diffusive flux density, J, at the surface of an isolated droplet is given by

$$J(\alpha) = J_0 \left\{ \frac{\sin \theta_c}{2} + \sqrt{2} \left(\cosh \alpha + \cos \theta_c \right)^{3/2} \right.$$
$$\left. \int_0^\infty \frac{\tau \cosh(\theta_c \tau)}{\cosh(\pi \tau)} \tanh[\tau(\pi - \theta_c)] P_{i\tau - 1/2} \left(\cosh \alpha \right) d\tau \right\}$$

(2)

In eq 2, (α, β) are the toroidal coordinates for an azimuthally symmetric droplet with contact radius (a) and contact angle (θ_c), $\beta = 3\pi - \theta_c$ on the droplet surface, $J_0 = D(C_s - C_\infty)/a$, D is the vapor diffusion coefficient, C_s is the saturation vapor concentration at the droplet surface, C_∞ is the ambient vapor concentration, $P_{i\tau - 1/2}$ is the Legendre function of complex degree, and τ is a dummy variable. The vapor concentration is $C(\alpha, \beta)$. The total evaporated mass flux for an isolated droplet is obtained by integrating $J(\alpha)$ over the droplet's surface:

$$-\left(\frac{dm}{dt} \right)_{\substack{\text{isolated} \\ \text{droplet}}} = \int_0^\infty J(\alpha) \frac{2\pi a^2 \sinh \alpha}{(\cosh \alpha + \cos \theta_c)^2} d\alpha$$

(3)

However, the presence of nearby droplets can significantly slow this evaporation rate. Instead of the zero flux Neumann

boundary condition along the substrate ($\beta = 2\pi$) for the isolated droplet case, nearby droplets impose the Dirichlet boundary condition $C = C_s$ at the surface of every neighboring droplet. Consequently, the solution for $C(\alpha,\beta)$ decays more gradually in the vicinity of the droplet under investigation. Thus, the evaporation rate is slowed because it is proportional to the gradient of C on the droplet surface. Moreover, the amount of slowdown varies across the droplet surface depending on the sizes of and distances to the nearby droplets.

We define the slowdown factor, SF, as the ratio of the measured evaporation rate dm/dt for the droplet under investigation in the spray to the evaporation rate predicted for an isolated droplet by eq 3. Using the Mehler−Fock integral transform to simplify eq 3 by writing the Bessel function as an integral and exchanging the order of integration (see Supporting Information of ref 66), we can quantify SF as

$$\mathrm{SF} \equiv \frac{\left(\frac{dm}{dt}\right)_{\text{measured}}}{\left(\frac{dm}{dt}\right)_{\substack{\text{isolated} \\ \text{droplet}}}}$$

$$= \frac{-\left(\frac{dm}{dt}\right)_{\text{measured}}}{J_0 \pi a^2 \left\{ \tan\frac{\theta_c}{2} + 8 \int_0^\infty \frac{\cosh^2(\theta_c \tau)}{\sinh(2\pi\tau)} \tanh[\tau(\pi - \theta_c)]\, d\tau \right\}}$$

(4)

SF is a purely geometrical factor that depends only on the distribution and shapes of the sprayed droplets. Although the ambient temperature and relative humidity can greatly affect the evaporation rate, their effect is normalized out because SF is a ratio, provided that the background temperature and humidity are the same for the sprayed droplet and isolated droplet. If the spray results in a single isolated droplet, then SF = 1.

Figure 8a shows the measured slowdown factor for the droplets of Figures 3−6, where we have used our measurements
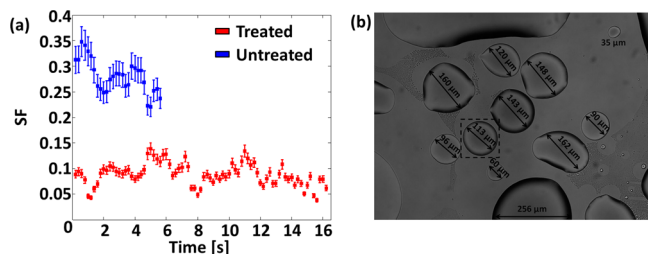

Figure 8. Evaporation slowdown. (a) Measured slowdown factor for the droplets of Figures 3 and 5. (b) Low magnification amplitude image showing a typical spray pattern on an untreated glass surface. In this case, 38% of the surface of the substrate is covered with water.

for dm/dt, θ_c, and a at each moment in time, used $\rho = 997$ kg/m^3, and computed J_0 using the following values: $T = 22\ °C$, $D = 2.49 \times 10^{-5}$ m^2/s, $C_s = 1.97 \times 10^{-2}$ kg/m^3, and $C_\infty = 9.26 \times 10^{-3}$ kg/m^3 (47% relative humidity). The error bars, which represent the standard deviation (SD) in a single measurement, are dominated by the uncertainty in temperature of $\pm 1\ °C$ and humidity of $\pm 3\%$, but also include an estimated uncertainty in dm/dt, θ_c, and a of $\pm 2\%$. The droplet on the treated surface slowed more, possibly due to a higher local droplet density during the spray.

Figure 8b is a low magnification amplitude image showing a typical spray pattern on an untreated surface. See the corresponding movie M11.[56] Notice the presence of submicrometer sized droplets around the perimeter of some droplets. Vapor from the larger droplets saturates the air above the submicrometer droplets and completely prevents them from evaporating. Because of this screening effect, the submicrometer droplets take the same amount of time to evaporate as the large droplet rather than evaporating in orders of magnitude shorter time as earlier theory would suggest. Theory for isolated droplets predicts that a small droplet evaporates faster than a larger one because the small droplet has a larger capillary pressure.[67] The droplets are in an open environment. The ambient above the droplets contains water vapor but it is not oversaturated because water vapor is lighter than air.[68] Therefore, all ideal droplets will eventually evaporate because they are never in thermodynamic equilibrium in this open system.[69] Nonideal droplets, that is, ones that trap impurities, can evaporate for a while and then stop once surface tension makes it thermodynamically unfavorable to continue evaporation. These behaviors can be seen in movie M11 in which the droplets evaporate until they become very small but they never fully disappear. In Figure 8b, the two-dimensional fill factor of water covering the slide is 38%, but notice the variation in the local droplet density and in the droplet sizes. If the geometries of all sprayed droplets on the substrate were measured and enormous computational resources were available, SF could be simulated by solving the diffusion equation numerically. Because this is impractical, we will construct three approximate models to better understand the data in Figure 8a. Let $c(x, y, z, t) = (C(x, y, z, t) - C_\infty)/(C_s - C_\infty)$ be the normalized vapor concentration; that is, c satisfies the diffusion equation with boundary conditions $c = 1$ on the droplet surface and $c = 0$ at infinity. We will compute $c(x, y, z, t)$ numerically using Comsol Multiphysics for an approximate spray distribution and for an isolated droplet. We then can compute dm/dt in both cases and divide the results to obtain a theoretical prediction for SF that we can compare to our experimental measurements in Figure 8a.

In the first model, we assume there are a small number of droplets and compute c in the steady state. Next, we compute the net diffusive flux integrated over the surface of the selected droplet of interest and divide by the integrated flux for the single droplet simulation. Figure 9a shows the simulation geometry for a single isolated droplet. Figure 9b shows the steady-state normalized vapor concentration for the isolated droplet and for two almost touching droplets. By computing the ratio of the net diffusive flux across the droplet of interest (located at the origin) for the two-droplet geometry to that for the one-droplet case, we find that the presence of the second droplet slows the evaporation rate of the first droplet with SF = 0.78. Simulations show that as more neighboring droplets are added, the concentration in the vicinity of the droplet of interest becomes more uniform. Thus, the evaporation rate continues to decrease and asymptotically approaches zero as the number of droplets approaches infinity even if the droplet density is arbitrarily low provided that it is nonzero. The first model is appropriate for predicting the measured SF when there are only a small number of droplets and their geometries are known. However, in the experiment, the spray randomly covers a large portion of the 50 mm × 22 mm coverslip, and so the simulation domain is too large for available computational resources. Thus, we will develop two other models that
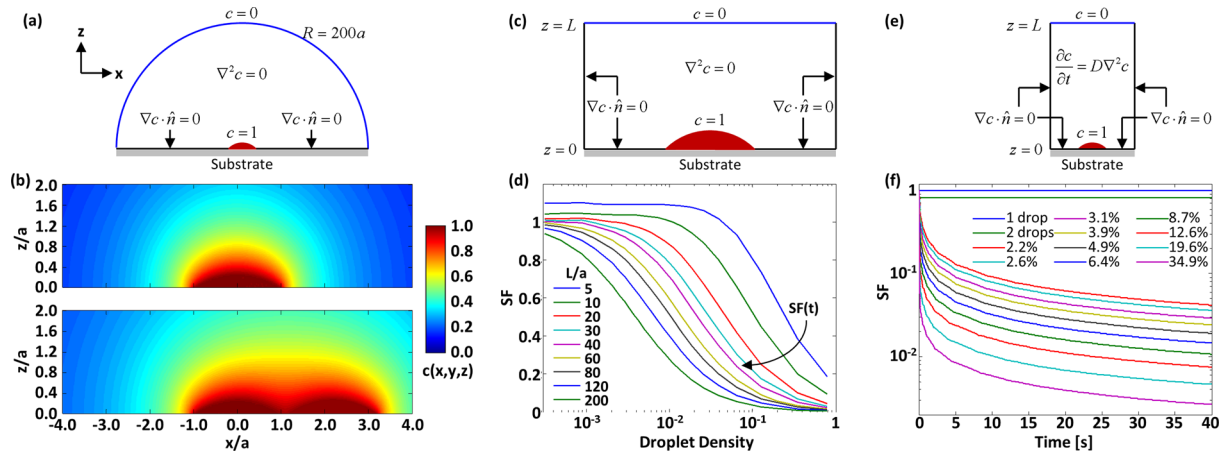
Figure 9. Theoretical models. (a) Cross-sectional view of the three-dimensional (x, y, z) simulation domain and boundary conditions for the steady-state model with a finite number of droplets. There is zero flux through the substrate. The outer boundary with $c = 0$ is a hemispherical shell of radius $200a$. (b) The normalized vapor concentration is simulated in the vicinity of a single droplet and two droplets. (c) Cross-sectional view of the three-dimensional (x, y, z) simulation domain and boundary conditions for the unit cell for the infinite rectangular array of droplets in steady state. The figure is drawn at a scale of droplet density = 8.7% and $L/a = 3$. (d) SF is simulated versus the droplet density for several distances L to the $c = 0$ boundary layer. The curved arrow shows a possible trajectory for SF(t). (e) Cross-sectional view of the four-dimensional (x, y, z, t) simulation domain and boundary conditions for the unit cell for the infinite rectangular array of droplets. The figure is drawn at a scale of droplet density = 8.7% and $L/a = 9$; however, $L/a = 2000$ is used in the simulations so that distance L is much larger than the distance that the vapor diffuses in 40 s. (f) The time dependence of SF is simulated for the case of a single isolated droplet (SF = 1), for two almost touching droplets (SF = 0.78), and for the infinite rectangular array of droplets for several different densities. For the single and two droplet cases, the boundary condition on the sidewalls was $c = 0$ instead of zero flux for the infinite droplet case, the width of the box in the x−y plane was set to $2000a$, and the height was set to $L/a = 1000$.

investigate the evaporation slowdown from an infinite rectangular array of identical droplets and interpret our experimental results in the context that the number of droplets is very large but finite.

For the infinite droplet array, we simulate a single rectangular prism unit cell. Because the array is infinite, symmetry dictates that there can be no net diffusive flux through the four sidewalls. In the second model, we assume steady state but place the $c = 0$ boundary at a small finite height $z = L$ above the substrate. Figures 9c and d show the simulation geometry and the steady-state values of SF for the infinite array of droplets as a function of the droplet density for various normalized distances, L/a, to the top boundary. The physical interpretation of this model is that it utilizes a relatively small computational domain to approximate the effect of a large but finite number of neighboring droplets. The $c = 0$ boundary prevents water vapor from droplets that are farther than a distance on the order of L away from reaching the droplet of interest. Note that the number of droplets that contribute to slowing the evaporation scales as L^2 and that SF approaches zero as L approaches infinity for all droplet densities. The steady-state approximation in the second model does not agree perfectly with the experiment primarily because the number of neighboring droplets considered should not be fixed but rather should increase from zero to the final value over time because there is a time delay for the diffusing vapor to reach the droplet of interest. Steady state is appropriate for a small number of closely spaced droplets where this diffusion delay time is negligible in comparison to the evaporation time. Nevertheless, SF(t) can be approximated as a trajectory such as the curved arrow drawn in Figure 9d. The trajectory jumps downward among the family of steady-state curves to allow the number of neighboring droplets to increase over time, and it also moves left and up along a single curve to allow the droplet density to decrease as the array evaporates. These two effects partially offset each other, resulting in a slowly varying SF(t).

In the third model, we compute the time-dependent normalized concentration for the infinite rectangular array. We place the $c = 0$ boundary very far away so that it does not influence the solution. Figures 9e and f show the simulation geometry and the time dependence of SF for the infinite array of droplets for various droplet densities assuming $a = 50 \ \mu m$ and $D = 2.49 \times 10^{-5} \ m^2/s$. The time axis is shown in seconds to directly match the experimental data, but can be renormalized for an arbitrary sized droplet using the dimensionless parameter $\tau = tD/a^2$. In Figure 9f, SF$(t) = 1$ for the single droplet is drawn for reference. For two droplets, SF(t) plummets almost instantaneously from SF$(0) = 1$ to reach its steady-state value of SF = 0.78. The other curves for the infinite rectangular droplet array show that SF(t) falls very quickly from SF$(0) = 1$, and then SF(t) continues to gradually decrease over time and asymptotes to zero. As explained previously, the spray occupies a finite area on the coverslip. Let t_0 be the time it takes for the vapor from the droplets at the farthest edge of the spray to diffuse and influence the droplet of interest. At the beginning, that is, $t < t_0$, SF should follow the curve SF(t) for the given starting density but then asymptotically approach a nonzero value given approximately by SF(t_0) because no farther droplets are available to continue slowing the evaporation. As the array evaporates, the droplet density decreases and the trajectory will jump upward among the family of curves. As before, this partially offsets the effect of increasing droplet number and results in a slowly varying SF(t).

These three theoretical models show that neighboring droplets can significantly reduce the total evaporation rate observed in microdroplet sprays as well as affect its temporal dependence. The primary conclusion of the theoretical analysis is that the observed slowdown factor of 0.2−0.4 for the treated sample and 0.05−0.15 for the untreated sample can be explained by the models. The actual droplet spray distribution clearly falls between the case of two isolated droplets (SF = 0.78 in Figure 9b) and infinitely many droplets in an array (SF

< 0.01 for 34.9% density in Figure 9f). We believe the effective droplet density near each measured droplet was between 10% and 50% and that the droplets covered an area between 2 mm × 2 mm and 10 mm × 10 mm. For these conditions, the appropriate value for L/a in Figure 9d ranges approximately between 20 and 100. The intervals for L/a and droplet density constrain the expected SF to the range 0.02−0.35 according to Figure 9d. Future studies should focus on validating the models more precisely by measuring the evaporation of uniform large area microdroplet arrays. A secondary conclusion from the theoretical analysis is that the models indicate that neighboring droplets can nonuniformly reduce the local evaporation rate across a droplet surface. This is evident in Figure 9b where the gradient of c, and thus the local evaporation rate, is smallest on the edge nearest to the neighboring droplet ($x/a = 1$, $z = 0$) and largest on the farthest edge ($x/a = -1$, $z = 0$). Nonuniform evaporation could be responsible for partial pinning. The phenomenon we described in this section is called "cooperative evaporation", and it is in accord with previous studies.[70−72]

VI. CONCLUSIONS

We demonstrated a technique for capturing the dynamics of droplet evaporation in real-time. Our method enables direct measurement of many of the important parameters that characterize the wetting and evaporation processes. The contact angles were accurately measured at each point along the droplet's edge. The gradient angle profiles were also computed to clearly illustrate changes in the hydrodynamics during evaporation. Time-dependent measurements of the volume, height, contact radius, contact angle, contact angle distribution, and mass flux density were reported for two separate time-lapses. These cases clearly indicate the three phases of evaporation reported in previous literature. Our DPM imaging system is flexible and robust enough to capture all of this information with a single method, and without relying on any a priori knowledge of the droplet's geometry. Finally, the cooperative evaporation was observed to produce nonuniform mass flux densities during evaporation and also to significantly reduce the evaporation rate. Three theoretical models were presented that approximate the experimental conditions and explain the observed slowdown factor in evaporation. Future studies should use a higher pixel count CCD to enable a wider field of view and characterization of multiple sprayed droplets. Some other interesting problems that can be investigated using this instrument include droplet shape deformation during laminar and chaotic microfluidic flow, capillary action, and reflow of heated photoresist, and perhaps study of colloidal particles on the interfaces of drying droplets.

ASSOCIATED CONTENT

Ⓢ Supporting Information

The Supporting Information is available free of charge on the ACS Publications website at DOI: 10.1021/acs.langmuir.5b02148.

> Figures of microlens verification, derivation of maximum measurable contact angle, movies of height map, gradient angle map, contact angle map, histogram of contact angles, and mass flux density map of pinned−depinned transition on treated glass and partial pinning on untreated glass, and a low magnification amplitude movie of evaporation on untreated glass (PDF)

Video of the height map of the droplet on treated glass as it transitions from being pinned to being depinned (AVI). Still images are shown in Figure 3a.

Video of the corresponding gradient angle map (AVI). Still images are shown in Figure 3b.

Video of the corresponding contact angle map (AVI). Still images are shown in Figure 3c.

Video of the corresponding contact angle distribution histogram (AVI). Still images are shown in Figure 3d.

Video of the height map of the droplet on untreated glass that experiences partial pinning (AVI). Still images are shown in Figure 5a.

Video of the corresponding gradient angle map (AVI). Still images are shown in Figure 5b.

Video of the corresponding contact angle map (AVI). Still images are shown in Figure 5c.

Video of the corresponding contact angle distribution histogram (AVI). Still images are shown in Figure 5d.

Video of the mass flux density of the droplet on treated glass (AVI). Still images are shown in Figure 7a.

Video of the mass flux density of the droplet on untreated glass (AVI). Still images are shown in Figure 7b.

Video of the evaporation of a typical spray pattern on untreated glass (AVI). Still images are shown in Figure 8b.

AUTHOR INFORMATION

Corresponding Author
*Phone: (217) 244-0799. E-mail: lgoddard@illinois.edu.

Present Addresses
[‖]Nanoscale and Quantum Optics Laboratory, Department of Applied Physics and Materials Science, California Institute of Technology, Pasadena, California 91125, United States.
[⊥]Department of Chemistry, University of Cambridge, Lensfield Road, Cambridge CB2 1EW, United Kingdom.
[#]School of Physics, Georgia Institute of Technology, Atlanta, Georgia 30332, United States.

Notes
The authors declare the following competing financial interest(s): G.P. is founder of Phi Optics, Inc., a company developing quantitative phase imaging technology for materials and life science applications.

ABBREVIATIONS

SCA, spherical cap approximation; RIM, reflectance interference microscopy; AFM, atomic force microscopy; ESEM, environmental scanning electron microscopy; TEM, transmission electron microscopy; DPM, diffraction phase microscopy; QPI, quantitative phase imaging; L, laser; SMF, single mode fiber; FC, fiber collimator; CL, collector lens; CON, condenser; S, sample; OBJ, objective; BS, beam splitter; TL, tube lens; G, grating; L1/L2, lenses; PF, pinhole filter; CCD, charge-coupled device; NA, numerical aperture; MFD, mass

flux density; J, evaporative flux density; SE, standard error; SD, standard deviation; SF, slowdown factor

■ REFERENCES

(1) Zimmermann, M.; Bentley, S.; Schmid, H.; Hunziker, P.; Delamarche, E. Continuous flow in open microfluidics using controlled evaporation. *Lab Chip* **2005**, *5* (12), 1355−1359.

(2) Thiele, J.; Windbergs, M.; Abate, A. R.; Trebbin, M.; Shum, H. C.; Forster, S.; Weitz, D. A. Early development drug formulation on a chip: Fabrication of nanoparticles using a microfluidic spray dryer. *Lab Chip* **2011**, *11* (14), 2362−2368.

(3) Bhushan, B.; Israelachvili, J. N.; Landman, U. Nanotribology: friction, wear, and lubrication at the atomic scale. *Nature* **1995**, *374*, 607−616.

(4) Blossey, R. Self-cleaning surfaces- virtual realities. *Nat. Mater.* **2003**, *2*, 301−306.

(5) Barberoglou, M.; Zorba, V.; Stratakis, E.; Spanakis, E.; Tzanetakis, P.; Anastasiadis, S. H.; Fotakis, C. Bio-inspired water repellent surfaces produced by ultrafast laser structuring of silicon. *Appl. Surf. Sci.* **2009**, *255*, 5425−5429.

(6) Jia, W.; Qiu, H. H. Experimental investigation of droplet dynamics and heat transfer in spray cooling. *Exp. Therm. Fluid Sci.* **2003**, *27* (7), 829−838.

(7) Daly, D.; Steven, R. F.; Hutley, M. C.; Davies, N. The manufacture of microlenses by melting photoresist. *Meas. Sci. Technol.* **1990**, *1*, 759−766.

(8) Thiele, U.; Mertig, M.; Pompe, W. Dewetting of an Evaporating Thin Liquid Film: Heterogeneous Nucleation and Surface Instability. *Phys. Rev. Lett.* **1998**, *80* (13), 2869−2872.

(9) Okuzono, T.; Ozawa, K. y.; Doi, M. Simple Model of Skin Formation Caused by Solvent Evaporation in Polymer Solutions. *Phys. Rev. Lett.* **2006**, *97*, 136103.

(10) Pauchard, L.; Allain, C. Stable and Unstable surface evolution during the drying of a polymer solution drop. *Phys. Rev. E: Stat. Phys., Plasmas, Fluids, Relat. Interdiscip. Top.* **2003**, *68* (5), 052801.

(11) Rabani, E.; Reichman, D. R.; Geissler, P. L.; Brus, L. E. Drying-mediated self-assembly of nanoparticles. *Nature* **2003**, *426*, 271−274.

(12) Nguyen, V. X.; Stebe, K. J. Patterning of small particles by a surfactant-enhanced Marangoni-Benard instability. *Phys. Rev. Lett.* **2002**, *88* (16), 164501.

(13) McHale, G. Surface free energy and microarray deposition technology. *Analyst* **2007**, *132* (3), 192−195.

(14) Kawase, T.; Sirringhaus, H.; Friend, R. H.; Shimoda, T. Inkjet printed via-hole interconnections and resistors for all-polymer transistor circuits. *Adv. Mater.* **2001**, *13* (21), 1601−1605.

(15) Hwang, S.-W.; Park, G.; Edwards, C.; Corbin, E. A.; Kang, S.-K.; Cheng, H.; Song, J.-K.; Kim, J.-H.; Yu, S.; Ng, J.; Lee, J. E.; Kim, J.; Yee, C.; Bhaduri, B.; Su, Y.; Omenetto, F. G.; Huang, Y.; Bashir, R.; Goddard, L.; Popescu, G.; Lee, K.-M.; Rogers, J. A. Dissolution Chemistry and Biocompatibility of Single-Crystalline Silicon Nano-membranes and Associated Materials for Transient Electronics. *ACS Nano* **2014**, *8* (6), 5843−5851.

(16) Sirringhaus, H.; Kawase, T.; Friend, R. H.; Shimoda, T.; Inbasekaran, M.; Wu, W.; Woo, E. P. High-resolution Inkjet Printing of All-Polymer Transistor Circuits. *Science* **2000**, *290* (5499), 2123−2126.

(17) Park, J.-U.; Hardy, M.; Kang, S. J.; Barton, K.; Adair, K.; Mukhopadhyay, D. k.; Lee, C. Y.; Strano, M. S.; Alleyne, A. G.; Georgiadia, J. G.; Ferreira, P. M.; Rodgers, J. A. High-resolution electrohydrodynamics jet printing. *Nat. Mater.* **2007**, *6*, 782−789.

(18) Hu, H.; Larson, R. G. Marangoni Effect Reverses Coffee-Ring Depositions. *J. Phys. Chem. B* **2006**, *110*, 7090.

(19) Murisic, N.; Kondic, L. On evaporation of sessile drops with moving contact lines. *J. Fluid Mech.* **2011**, *679*, 219−246.

(20) Yunker, P. J.; Still, T.; Lohr, M. A.; Yodh, A. G. Supresion of the coffee-ring by shape-dependent capillary interactions. *Nature* **2011**, *476*, 308−311.

(21) McHale, G.; Newton, M. I. Frenkel's method and the dynamic wetting of heterogeneous planar surfaces. *Colloids Surf., A* **2002**, *206* (1−3), 193−201.

(22) Erbil, H. Y.; McHale, G.; Newton, M. I. Drop Evaporation on Solid Surfaces: Constant Contact Angle Mode. *Langmuir* **2002**, *18* (7), 2636−2641.

(23) Hu, H.; Larson, R. G. Evaporation of a Sessile Droplet on a Substrate. *J. Phys. Chem. B* **2002**, *106* (6), 1334−1344.

(24) Picknett, R. G.; Bexon, R. The Evaporation of Sessile or Pendant Drops in Still Air. *J. Colloid Interface Sci.* **1977**, *61* (2), 336−350.

(25) Lebedev, N. N. *Special Functions and Their Application*; Prentice Hall: Englewood Cliffs, NJ, 1965.

(26) Guena, G.; Poulard, C.; Cazabat, A. M. The Contact Angle of Droplets Evaporating at Ambient Temperature. *Applied Mathematics Research Express* **2006**, 1−16.

(27) Dhavaleswarapu, H. K.; Migliaccio, C. P.; Garimella, S. V.; Murthy, J. Y. Experimental investigation of evaporation from low-contact-angle sessile droplets. *Langmuir* **2010**, *26* (2), 880−888.

(28) Gokhale, S. J.; Plawsky, J. L.; Wayner, P. C. Experimental investigation of contact angle, curvature, and contact line motion in dropwise condensation and evaporation. *J. Colloid Interface Sci.* **2003**, *259* (2), 354−366.

(29) Chen, J.-D.; Wada, N. Edge profiles and dynamic contact angles of a spreading drop. *J. Colloid Interface Sci.* **1992**, *148* (1), 207−222.

(30) de Ruiter, J.; Oh, J. M.; van den Ende, D.; Mugele, F. Dynamics of Collapse of Air Films in Drop Impact. *Phys. Rev. Lett.* **2012**, *108* (7), 074505.

(31) van der Veen, R. C. A.; Tran, T.; Lohse, D.; Sun, C. Direct measurements of air layer profiles under impacting droplets using high-speed color interferometry. *Phys. Rev. E* **2012**, *85* (2), 026315.

(32) Hoang, A.; Kavehpour, H. P. Dynamics of nanoscale precursor film near a moving contact line of spreading drops. *Phys. Rev. Lett.* **2011**, *106*, 254501.

(33) Hoang, A.; Berteloot, G.; Sharif-Kashani, P.; Kavehpour, H. P. Dynamic measurement of microfilms and nanofilms of fluids using fluorescence microscopy. *Exp. Fluids* **2012**, *52* (6), 1657−1662.

(34) Pompe, T.; Herminghaus, S. Three-Phase Contact Line Energetics from Nanoscale Liquid Surface Topographies. *Phys. Rev. Lett.* **2000**, *85* (9), 1930−1933.

(35) Mugele, F.; Becker, T.; Nikopoulos, R.; Kohonen, M.; Herminghaus, S. Capillarity at the nanoscale: an AFM view. *J. Adhes. Sci. Technol.* **2002**, *16* (7), 951−964.

(36) Checco, A.; Schollmeyer, H.; Daillant, J.; Guenoun, P.; Boukherroub, R. Nanoscale Wettability of Self-Assembled Monolayers Investigated by Noncontact Atomic Force Microscopy. *Langmuir* **2006**, *22* (1), 116−126.

(37) Danilatos, G. The examination of fresh or living plant material in an environmental scanning electron microscope. *J. Microsc.* **1981**, *121* (2), 235−238.

(38) Rykaczewski, K. Microdroplet Growth Mechanism during Water Condensation on Superhydrophobic Surfaces. *Langmuir* **2012**, *28* (20), 7720−7729.

(39) Paxson, A. T.; Varanasi, K. K. Self-similarity of contact line depinning from textured surfaces. *Nat. Commun.* **2013**, *4*, 1492.

(40) Liu, Q.; Leong, F. Y.; Aabdin, Z.; Anand, U.; Si Bui Quang, T.; Mirsaidov, U. Nanodroplet Depinning from Nanoparticles. *ACS Nano* **2015**, *9*, 9020.

(41) Edwards, C.; Arbabi, A.; Popescu, G.; Goddard, L. L. Optically monitoring and controlling nanoscale topography during semi-conductor etching. *Light: Sci. Appl.* **2012**, *1*, e30.

(42) Debnath, S. K.; Park, Y. Real-time quantitative phase imaging with a spatial phase-shifting algorithm. *Opt. Lett.* **2011**, *36* (23), 4677−4679.

(43) Pham, H.; Ding, H.; Sobh, N.; Do, M.; Patel, S.; Popescu, G. Off-axis quantitative phase imaging processing using CUDA: toward real-time applications. *Biomed. Opt. Express* **2011**, *2* (7), 1781−1793.

(44) Edwards, C.; Wang, K.; Zhou, R.; Bhaduri, B.; Popescu, G.; Goddard, L. L. Digital projection photochemical etching defines gray-scale features. *Opt. Express* **2013**, *21* (11), 13547−13554.

(45) Edwards, C.; Bhaduri, B.; Nguyen, T.; Griffin, B.; Pham, H.; Kim, T.; Popescu, G.; Goddard, L. L. Effects of spatial coherence in diffraction phase microscopy. *Opt. Express* **2014**, *22* (5), 5133−5146.

(46) Zhou, R.; Edwards, C.; Arbabi, A.; Popescu, G.; Goddard, L. L. Detecting 20 nm wide defects in large area nanopatterns using optical interferometric microscopy. *Nano Lett.* **2013**, *13* (8), 3716−3721.

(47) Bhaduri, B.; Edwards, C.; Pham, H.; Zhou, R.; Nguyen, T.; Goddard, L.; Popescu, G. Diffraction phase microscopy: principles and applications in materials and life sciences. *Adv. Opt. Photonics* **2014**, *6* (1), 57−119.

(48) Edwards, C.; Zhou, R.; Hwang, S.-W.; McKeown, S. J.; Wang, K.; Bhaduri, B.; Ganti, R.; Yunker, P. J.; Yodh, A. G.; Rogers, J. A.; Goddard, L. L.; Popescu, G. Diffraction phase microscopy: monitoring nanoscale dynamics in materials science [Invited]. *Appl. Opt.* **2014**, *53* (27), G33−G43.

(49) Edwards, C.; Bhaduri, B.; Griffin, B. G.; Goddard, L. L.; Popescu, G. Epi-illumination diffraction phase microscopy with white light. *Opt. Lett.* **2014**, *39* (21), 6162−6165.

(50) Edwards, C.; McKeown, S. J.; Zhou, J.; Popescu, G.; Goddard, L. L. In situ measurements of the axial expansion of palladium microdisks during hydrogen exposure using diffraction phase microscopy. *Opt. Mater. Express* **2014**, *4* (12), 2559−2564.

(51) Popescu, G. *Quantitative Phase Imaging of Cells and Tissues*; McGraw-Hill: New York, 2011.

(52) Bhaduri, B.; Pham, H.; Mir, M.; Popescu, G. Diffraction phase microscopy with white light. *Opt. Lett.* **2012**, *37* (6), 1094−1096.

(53) Popescu, G.; Ikeda, T.; Dasari, R.; Feld, M. S. Diffraction phase microscopy for quantifying cell structure and dynamics. *Opt. Lett.* **2006**, *31* (6), 775−777.

(54) Pham, H. V.; Edwards, C.; Goddard, L. L.; Popescu, G. Fast phase reconstruction in white light diffraction phase microscopy. *Appl. Opt.* **2013**, *52* (1), A97−A101.

(55) Mack, G. L. The Determination of Contact Angles from Measurements of the Dimensions of Small Bubbles and Drops. I. The Spheroidal Segment Method for Acute Angles. *J. Phys. Chem.* **1935**, *40* (2), 159−167.

(56) See the Supporting Information for further details including additional measurements and videos.

(57) Barer, R. Determination of Dry Mass, Thickness, Solid and Water Concentration in Living Cells. *Nature* **1953**, *172* (4389), 1097−1098.

(58) Popescu, G.; Park, Y.; Lue, N.; Best-Popescu, C.; Deflores, L.; Dasari, R. R.; Feld, M. S.; Badizadegan, K. Optical imaging of cell mass and growth dynamics. *American Journal of Physiology - Cell Physiology* **2008**, *295* (2), C538−C544.

(59) Shanahan, M. E. R.; Bourges, C. Effects of evaporation on contact angles on polymer surfaces. *Int. J. Adhes. Adhes.* **1994**, *14* (3), 201−205.

(60) Bourges-Monnier, C.; Shanahan, M. E. R. Influence of Evaporation on Contact Angle. *Langmuir* **1995**, *11*, 2820−2829.

(61) Shin, D. H.; Lee, S. H.; Jung, J.-Y.; Yoo, J. Y. Evaporating characteristics of sessile droplet on hydrophobic and hydrophilic surfaces. *Microelectron. Eng.* **2009**, *86* (4−6), 1350−1353.

(62) Deegan, R. D.; Bakajin, O.; Dupont, T. F.; Huber, G.; Nagel, S. R.; Witten, T. A. Capillary flow as the casue of ring stains from dried liquid drops. *Nature* **1997**, *389*, 827−829.

(63) Deegan, R. D.; Bakajin, O.; Dupont, T. F.; Huber, G.; Nagel, S. R.; Witten, T. A. Contact line deposits in an evaporating drop. *Phys. Rev. E: Stat. Phys., Plasmas, Fluids, Relat. Interdiscip. Top.* **2000**, *62* (1), 756−765.

(64) Rowan, S. M.; Newton, M. I.; McHale, G. Evaporation of Microdroplets and the Wetting of Solid Surfaces. *J. Phys. Chem.* **1995**, *99* (35), 13268−13271.

(65) Nguyen, T. A. H.; Nguyen, A. V.; Hampton, M. A.; Xu, Z. P.; Huang, L. B.; Rudolph, V. Theoretical and experimental analysis of droplet evaporation on solid surfaces. *Chem. Eng. Sci.* **2012**, *69* (1), 522−529.

(66) Nguyen, T. A. H.; Nguyen, A. V. On the Lifetime of Evaporating Sessile Droplets. *Langmuir* **2012**, *28* (3), 1924−1930.

(67) Butt, H.-J.; Golovko, D. S.; Bonaccurso, E. On the Derivation of Young's Equation for Sessile Drops: Nonequilibrium Effects Due to Evaporation. *J. Phys. Chem. B* **2007**, *111* (19), 5277−5283.

(68) Shahidzadeh-Bonn, N.; Rafai, S.; Azouni, A.; Bonn, D. Evaporating droplets. *J. Fluid Mech.* **2006**, *549*, 307−313.

(69) Toshev, B. V.; Avramov, M. Z. On the thermodynamic stability of small droplets at positive line tension. *Colloids Surf., A* **1993**, *75*, 33−37.

(70) Weijs, J. H.; Lohse, D. Why Surface Nanobubbles Live for Hours. *Phys. Rev. Lett.* **2013**, *110* (5), 054501.

(71) Schäfle, C.; Leiderer, P.; Bechinger, C. Subpattern formation during condensation processes on structured substrates. *EPL (Europhysics Letters)* **2003**, *63* (3), 394−400.

(72) Tolédano, P.; Mettout, B.; Aroyo, M.; Perez Mato, J. M. Theory of the Cooperative Evaporation of Volatile Droplets. *Phys. Rev. Lett.* **2005**, *95* (20), 205701.